Journal of Marine Science and Technology

Volume 22 | Issue 2 Article 16

DYNAMICS AND CUTTING STABILITY OF DYNAMICALLY LOADED WORKTABLE SUBJECTED TO ELASTIC SUPPORTS

Kuo-Chiang Cha
Department of Mechanical Engineering, Chang Gung University, Tao-Yuan, Taiwan, R.O.C., ckc001@mail.cgu.edu.tw

Nenzi Wang
Department of Mechanical Engineering, Chang Gung University, Tao-Yuan, Taiwan, R.O.C.

Jen-Yi Liao
Chung-Shan Institute of Science and Technology, Tao-Yuan, Taiwan, R.O.C

DYNAMICS AND CUTTING STABILITY OF DYNAMICALLY LOADED WORKTABLE SUBJECTED TO ELASTIC SUPPORTS

Acknowledgements

This work was supported by the National Science Council of, the Republic of China, under the contract number: NSC 100-2221-E-182-045.

Journal of Marine Science and Technology, Vol. 22, No. 2, pp. 247-258 (2014)
DOI: 10.6119/JMST-013-0905-1

DYNAMICS AND CUTTING STABILITY OF DYNAMICALLY LOADED WORKTABLE SUBJECTED TO ELASTIC SUPPORTS

Kuo-Chiang Cha[1], Nenzi Wang[1], and Jen-Yi Liao[2]

Key words: dynamically loaded worktable, assumed mode expansion, stability lobe diagram, the maximum negative real part of the overall dynamic compliance.

ABSTRACT

This paper investigated the dynamic characteristics and the cutting stability of a dynamically loaded worktable on elastic supports in a surface grinder. The operation of worktables is usually dynamically loaded in various positions, which results in a complex system of governing equations. In this study, the assumptions of elastic and rigid body modes of a free-free beam were specified in analyzing the worktable. By combining the Lagrange energy method with the technique of assumed mode expansion, the system of equations was developed. The absolute value of the maximum negative real part of the overall dynamic compliance (MNRPODC) and the limiting chip width were used as the performance indicators to evaluate the structural characteristics of the worktable during simulated machining. The 3D stability lobe diagram was then computed. The cutting stability was verified by comparing the results obtained in time-domain analysis with the lobe diagram. The procedure presented in this study to improve the dynamics performance of a surface grinder can also be implemented in a similar fashion for many other machine tool applications.

I. INTRODUCTION

A machine tool is a complex mechanical system in which the machining performance is closely related to the tool's dynamic characteristics. Metal cutting usually causes excess vibration between the workpiece and the cutting tool which is known as machine tool chatter. The machine tool chatter, with its self-excited vibration caused and sustained by the cutting force during the cutting process, can cause severe adverse effects on the workpiece surface precision and reduce tool lifetime. Therefore, a machine tool with adequate static and dynamic characteristics can promote the machined precision of workpieces while ensure the safety, stability, and reliability of the machine tool.

In the literature [1, 14, 15, 17, 19] researchers usually use the width of cut (b_{lim}) under no chatter condition (i.e., maximum stability) as the dynamic performance indicator in the analysis for a machine tool. For instance, Tlusty [16] proposed that b_{lim} in the stability analysis of regenerative chatter vibration is determined by the absolute value of the Maximum Negative Real Part of the Overall Dynamic Compliance (MNRPODC); that is, $b_{lim} = 1/(2 \times K_f \times |\text{MNRPODC}|)$, where K_f is the cutting stiffness per unit width of cut. In a system the cutting stability is inversely proportional to the |MNRPODC|. This study, therefore, applied b_{lim} to evaluate the cutting stability of the dynamically loaded non-rigid worktable on elastic supports.

The dynamic response of a beam structure (non-rotating structure) due to moving loads has been used to predict the dynamic behavior of vehicles when traveling on bridge structures [12, 13] The analysis is an analogy to the loading of machine tool's worktable. On the other hand, the effects of moving loads on rotating shafts or structure are studied. For example, Katz *et al*. [10] investigated the dynamic response of a beam model, based on the Euler, Rayleigh and Timoshenko theories. The beam is loaded with a constant velocity moving force. Argento and Scott [3] generalized Katz's procedure to a rotating beam subjected to an accelerating distributed surface force. Gu *et al*. [7] applied the analysis procedure to the study of dynamic characteristics of the ball-screw feed drive system in a machine tool. In addition, many studies on the stiffness or structural vibrations and optimization of machine tools have been conducted by experimental, analytical, or numerical methods in past decades. Among these researchers, Yoshimura [20, 21] accomplished substantial analyses on the structural dynamic for machine tools. Zhang, *et al*. [22] applied CAE (Computer Aided Engineering) techniques to predict the overall structural dynamic characteristics. They conclude that the vibration on the weaker segment of the structure has a significant effect on the dynamic instability of

Paper submitted 01/21/13; revised 08/01/13; accepted 09/05/13. Author for correspondence: Kuo-Chiang Cha (e-mail: ckc001@mail.cgu.edu.tw).
[1] Department of Mechanical Engineering, Chang Gung University, Tao-Yuan, Taiwan, R.O.C.
[2] Chung-Shan Institute of Science and Technology, Tao-Yuan, Taiwan, R.O.C.

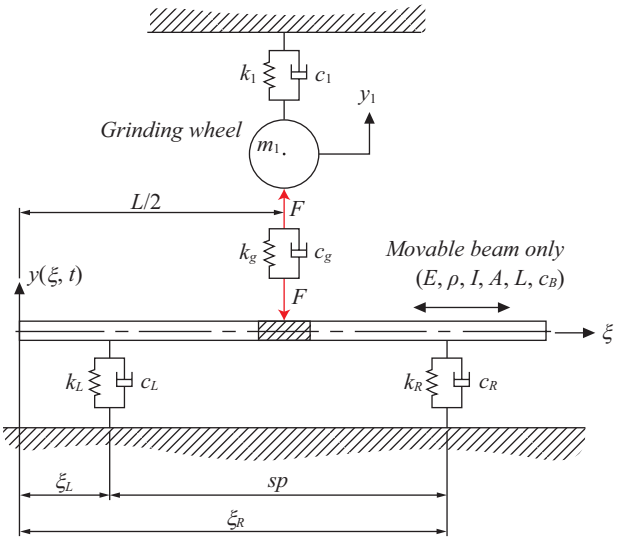

Fig. 1. Worktable model on elastic supports at various positions.

a machine tool. In recent years, the authors have applied theories to develop different models of surface grinder, such as the lumped-mass parametric model with eight degrees of freedom and the elastic-supported rigid-worktable model with three degrees of freedom. To achieve the goal of improving overall dynamic performance and cutting stability, the former model is constructed to a prediction model for the structural stability using back propagation neural network [8], the latter model is used to study the dynamic characteristics and the cutting stability of the dynamically loaded rigid worktable on elastic supports [4]. Furthermore, there are rarely studies on the structural dynamic characteristics and cutting stability analysis of the non-rigid worktable with the elastic-supported due to variable-positions of the worktable.

II. BASIC THEORY

The model used for analyzing the dynamically loaded worktable on elastic supports is shown in Fig. 1. The worktable is modeled as an elastic beam sitting over the elastic supports separated by a span sp, where the spring and damping constants of the left and the right supports are k_L, c_L, k_R and c_R, respectively. It is assumed that the vibration in the vertical direction (direction y) affects the machining precision most; thus, only the motion in that direction was considered in this study. The surface grinder model consists of two parts: a grinding wheel and a worktable module. The former is composed of a grinding wheel (m_1), and a bearing supported spindle (k_1 and c_1). The latter is modeled by a free-free beam with elastic supports. The contact stiffness between the grinding wheel and the elastic beam is k_g and the contact damping is c_g. The coordinate of the worktable is denoted by ξ. In the simulation the cutting point is located initially at $\xi = L/2$ as start of machining, and the model is similar to a bridge model where a single-axle vehicle is moving over the cross-pier but opposite movement mechanism. In the past there were many models being proposed regarding the dynamics coupling response of vehicles moving on a simply supported bridge [5, 6, 9]. The model developed in this study is similar to these proposed models, except that the two ends of the span are supported on elastic support. The equations of the system are derived based on the technique of assumed mode expansion, in which the n elastic modes of the free-free beam and the two rigid body modes (translation and rotation) on the plane for the worktable are superposed, with the combination of other parts in the system. The derivation and methods developed are not commonly used in the past literature; therefore, the derivation is first verified by comparing the dynamic response of the rigid worktable model [4], also developed by the author, before applying the developed model to the analysis of structural static and dynamic characteristics and cutting stability of the dynamically loaded worktable at different positions during machining.

1. Modelling and Formulation [10]

Assume that the worktable is based on the Euler-Bernoulli beam theory with free-free conditions, where the beam is of uniform-section homogenous material with length L, and E is the Young's modulus of the beam, ρ is the density, A is the cross-section area, I is the area moment of inertia of the beam's cross section, and c_B is the beam damping. The differential equation for the transverse free vibration at various positions and time is as follows:

$$\frac{\partial^2}{\partial \xi^2}\left(EI\frac{\partial^2 y}{\partial \xi^2}\right)+c_B\frac{\partial y}{\partial t}+\rho A\frac{\partial^2 y}{\partial t^2}=0. \tag{1}$$

For the free-free boundary conditions the moment and the shear stress at the both ends of the worktable are set to zero, i.e., $y''(0, t) = 0$, $y''(L, t) = 0$, $y'''(0, t) = 0$, $y'''(L, t) = 0$. In the assumed modes method, the solution of the free vibration problem is approximated by a linear combination of n admissible functions, $\phi_i(\xi)$, as

$$y(\xi, t)=\sum_{i=1}^{n}\phi_i(\xi)q_i(t).$$

where $q_i(t)$ are time dependent generalized coordinates.

Therefore, the normalized eigenfunction $\phi_i(\xi)$ from Eq. (1) can be obtained as follows:

$$\phi_i(\xi)=1/\sqrt{L}\left\{\cosh(\lambda_i\xi/L)+\cos(\lambda_i\xi/L)-\sigma_i\left[\sinh(\lambda_i\xi/L)+\sin(\lambda_i\xi/L)\right]\right\},\quad i=1, 2, \cdots, n. \tag{2}$$

Where,

$$\cos\lambda_i\cdot\cosh\lambda_i=1,\ \sigma_i=\frac{\cosh\lambda_i-\cos\lambda_i}{\sinh\lambda_i-\sin\lambda_i}.$$

Table 1. Value of λ_i associated with each normal mode.

Mode number (i)	Value of λ_i
1	4.730040744862704
2	7.853204624095837
3	10.995607838001671
4	14.137165491257464
5	17.278759657399480
…	…
n	$(n + 0.5)\,\pi$

Here, Table 1 shows value of λ_i associated with each mode.

The two normalized rigid body modes (translation and rotation) of a free-free beam on a plane can be expressed as follows:

$$\phi_H(\xi)=\frac{1}{\sqrt{L}};\quad \phi_S(\xi)=\sqrt{\frac{12}{L}}\left(\frac{\xi}{L}-\frac{1}{2}\right). \tag{3}$$

Use assumed mode expansion approach to combine the n free-free elastic beam modes in Eq. (2) and the generalized coordinates of the two rigid body modes in Eq. (3), $y(\xi, t)$ can be expressed as follows:

$$y(\xi,t)=\sum_{i=1}^{n}\phi_i(\xi)q_i(t)+\phi_S(\xi)q_S(t)+\phi_H(\xi)q_H(t). \tag{4}$$

Before the system equations can be derived by using the Lagrange method, the kinetic energy T, the potential energy U, and the dissipative energy R should be expressed as follows:

$$T=\frac{1}{2}\left[m_1\dot{y}_1^2(t)+\int_0^L\rho A\dot{y}^2(\xi,t)d\xi\right],$$

$$U=\frac{1}{2}\Big\{k_1y_1^2(t)+k_g\left[y_1(t)-y(\xi,t)\right]^2 +k_Ry^2(\xi_R,t)+k_Ly^2(\xi_L,t)+\int_0^L EI\,\ddot{y}^2(\xi,t)d\xi\Big\},$$

$$R=\frac{1}{2}\Big\{c_1\dot{y}_1^2(t)+c_g\left[\dot{y}_1(t)-\dot{y}(\xi,t)\right]^2 +c_R\dot{y}^2(\xi_R,t)+c_L\dot{y}^2(\xi_L,t)+\int_0^L c_B\dot{y}^2(\xi,t)d\xi\Big\}. \tag{5}$$

The Lagrange equations can be expressed as:

$$\frac{d}{dt}\left(\frac{\partial T}{\partial\dot{y}_1(t)}\right)-\frac{\partial(T-U)}{\partial y_1(t)}+\frac{\partial R}{\partial\dot{y}_1(t)}=0,$$

$$\frac{d}{dt}\left(\frac{\partial T}{\partial\dot{q}_i(t)}\right)-\frac{\partial(T-U)}{\partial q_i(t)}+\frac{\partial R}{\partial\dot{q}_i(t)}=0,\quad i=1,2,...,n. \tag{6}$$

Assume that the grinding wheel maintains contact with the worktable and there exists a unit force (F = 1) with equal magnitude but opposite direction between the tool and the workpiece, when the dynamically loaded worktable on elastic supports is moving [1, 16]. By using "VariationalCalculus" library in Maple software [18], one can derive the equations of motion for the discretized with n + 3 degree-of-freedom system on various worktable positions (ξ). These equations can be expressed in a matrix form as:

$$[M]\{\ddot{\gamma}_1\}+[C]\{\dot{\gamma}_1\}+[K]\{\gamma_1\}=\{f\}=\{\psi\} \tag{7}$$

where [M], [K], and [C] denote mass, stiffness and damping matrices, respectively. And

$$\{\gamma_1\}^T=\{y_1, q_1, q_2, \cdots, q_n, q_H, q_S\},$$

$$\{f\}^T=\{\psi(\xi)\}^T=\{-1, \phi_1(\xi), \phi_2(\xi), \cdots, \phi_n(\xi), \phi_H(\xi), \phi_S(\xi)\}.$$

All the derived elements in the matrices are summarized as follows:

a) The parametric expression of elements in mass matrix [M]:

$$[M]=\mathrm{diag}\left(\{m_1, \rho A, \rho A, \cdots, \rho A\}\right). \tag{8}$$

b) The parametric expression of elements in stiffness matrix [K]:

$$[K]=\begin{bmatrix} k_1+k_g & sym & sym & \cdots & sym & sym & sym \\ -k_g\phi_1(\xi) & B_{1,1} & B_{1,2} & \cdots & B_{1,n} & B_{1,H} & B_{1,S} \\ -k_g\phi_2(\xi) & sym & B_{2,2} & \cdots & B_{2,n} & B_{2,H} & B_{2,S} \\ \vdots & \vdots & \vdots & \vdots & \vdots & \vdots & \vdots \\ -k_g\phi_n(\xi) & sym & sym & \cdots & B_{n,n} & B_{n,H} & B_{n,S} \\ -k_g\phi_H(\xi) & sym & sym & \cdots & sym & B_{H,H} & B_{H,S} \\ -k_g\phi_S(\xi) & sym & sym & \cdots & sym & sym & B_{S,S} \end{bmatrix}. \tag{9}$$

Here

$$B_{jk}=\delta_{jk}S_{k,k}+k_g\phi_j(\xi)\phi_k(\xi)+k_R\phi_j(\xi_R)\phi_k(\xi_R) +k_L\phi_j(\xi_L)\phi_k(\xi_L);\quad j,k=1,2,...,n+2.$$

$\delta_{j,k}$ is the Kronecker delta function, which is denoted by $\delta_{j,k}=0, j\neq k$, and $\delta_{j,k}=1, j=k$. Where

$$[S]=\mathrm{diag}\left(\{k_1, S_{1,1}, S_{2,2}, \cdots, S_{n,n}, 0, 0\}\right),$$

$$S_{k,k}=EI(\lambda_i/L)^4,\quad k=1,2,\cdots,n.$$

The equations of tie and support vectors are defined as follows:
Tie vector:

$$\{\psi(\xi)\}^T = \{-1, \phi_1(\xi), \phi_2(\xi), \cdots, \phi_n(\xi), \phi_H(\xi), \phi_S(\xi)\}.$$

Support vector:

$$\{\kappa(\xi)\}^T = \{0, \phi_1(\xi), \phi_2(\xi), \cdots, \phi_n(\xi), \phi_H(\xi), \phi_S(\xi)\}$$

$$[K_0] = k_R\{\kappa(\xi_R)\}\{\kappa(\xi_R)\}^T + k_L\{\kappa(\xi_L)\}\{\kappa(\xi_L)\}^T + \text{diag}\left(\{k_1, S_{1,1}, \cdots, S_{n,n}, 0, 0\}\right),$$

$$[K] = [K_0] + k_g\{\psi(\xi)\}\{\psi(\xi)\}^T.$$

In the case of a free-free beam, if $\lambda = 0$ a rigid-body mode is resulted, i.e.,

$$S_{H,H} = S_{(n+1),(n+1)} = S_{S,S} = S_{(n+2),(n+2)} = 0.$$

The terms in $[K_0]$ are time invariant, and the second term of $[K]$ is time dependent.

c) The parametric expression of elements in damping matrix $[C]$

$$[C] = \begin{bmatrix} c_1 + c_g & sym & sym & \cdots & sym & sym & sym \\ -c_g\phi_1(\xi) & G_{1,1} & G_{1,2} & \cdots & G_{1,n} & G_{1,H} & G_{1,S} \\ -c_g\phi_2(\xi) & sym & G_{2,2} & \cdots & G_{2,n} & G_{2,H} & G_{2,S} \\ \vdots & \vdots & \vdots & \vdots & \vdots & \vdots & \vdots \\ -c_g\phi_n(\xi) & sym & sym & \cdots & G_{n,n} & G_{n,H} & G_{n,S} \\ -c_g\phi_H(\xi) & sym & sym & \cdots & sym & G_{H,H} & G_{H,S} \\ -c_g\phi_S(\xi) & sym & sym & \cdots & sym & sym & G_{S,S} \end{bmatrix} \quad (10)$$

Here

$$G_{jk} = \delta_{jk}c_B + c_g\phi_j(\xi)\phi_k(\xi) + c_R\phi_j(\xi_R)\phi_k(\xi_R) + c_L\phi_j(\xi_L)\phi_k(\xi_L), \quad j, k = 1, 2, ..., n+2.$$

$$[C_0] = c_R\{\kappa(\xi_R)\}\{\kappa(\xi_R)\}^T + c_L\{\kappa(\xi_L)\}\{\kappa(\xi_L)\}^T + \text{diag}\left(\{c_1, c_B, \cdots, c_B\}\right),$$

$$[C] = [C_0] + c_g\{\psi(\xi)\}\{\psi(\xi)\}^T.$$

Where c_B is beam damping, and note that the damping in a rigid body modes cannot be neglected, which may affect the system response significantly. Also noted that the terms in $[C_0]$ are time invariant, and the second term of $[C]$ is time dependent.

2. State-Space Representation of the System [23]

A state space model is a set of first-order differential equations composed of state variables and system input and output by which the motion state is described. The construction of a state space model facilitates the time domain and frequency domain analysis based on the system identification toolbox in Matlab. In this study, $\{\gamma\}$ is the state vector as Eq. (11):

$$\{\gamma\} = \begin{Bmatrix} \gamma_1 \\ \dot{\gamma}_1 \end{Bmatrix}. \quad (11)$$

Substitute Eq. (11) into Eq. (7), the state equation can be expressed as:

$$\{\dot{\gamma}\} = \underbrace{\begin{bmatrix} 0 & I \\ -M^{-1}K & -M^{-1}C \end{bmatrix}}_{[A_c]_{(2n+6)\times(2n+6)}}\{\gamma\} + \underbrace{\begin{Bmatrix} 0 \\ M^{-1}\psi \end{Bmatrix}}_{\{B_c\}_{(2n+6)\times 1}}. \quad (12)$$

The response between the tool and the workpiece at different worktable positions can then be expressed as follows:

$$r(\xi, t) = \{\psi(\xi)\}^T\{\gamma_1\} = \phi_S(\xi)q_S(t) + \phi_H(\xi)q_H(t) + \sum_{i=1}^{n}\phi_i(\xi)q_i(t) - y_1(t). \quad (13)$$

By combining Eqs. (12) and (13) one can obtain the state equation and the response equation simultaneously as follows:

$$\begin{cases} \{\dot{\gamma}(t)\} = [A_c]\{\gamma(t)\} + [B_c]\{f(t)\} \\ \{r(t)\} = [C_c]\{\gamma(t)\} + [D_c]\{f(t)\} \end{cases} \quad (14)$$

where

$$[A_c] = \begin{bmatrix} 0 & I \\ -M^{-1}K & -M^{-1}C \end{bmatrix}, [B_c] = \begin{bmatrix} 0 \\ M^{-1}\psi \end{bmatrix},$$

$$[C_c] = \begin{bmatrix} \psi^T & 0 \end{bmatrix}, [D_c] = [0].$$

When calculating the accurate system dynamic compliance between the tool and the workpiece, some mechanism should be provided to properly adjust the frequency step surrounding the structural natural and the anti-resonant frequency, so that the maximum negative real part of the overall dynamic compliance can be computed by using the matrices $[A_c]$, $[B_c]$, $[C_c]$ and $[D_c]$.

A Matlab command, ss2tf, can convert the state equations to a transfer function for any given input. The eigenvalues and

the eigenvectors of the matrix $[A_c]$ are the mode characteristics of the structural system. It is well known that a continuous time state space can be expanded to a discrete-time state space by sampling. If Δt is the sampling time interval in the analog-to-digital conversion, then the vectors in Eq. (14) can be discretized as follows:

$$\{\gamma_k\} = \begin{Bmatrix} \gamma_{1k} \\ \dot{\gamma}_{1k} \end{Bmatrix} = \begin{Bmatrix} \gamma_1(k\Delta t) \\ \dot{\gamma}_1(k\Delta t) \end{Bmatrix},$$

$$\{\psi_k\} = \{\psi(k\Delta t)\},\ \{r_k\} = \{r(k\Delta t)\}. \qquad (15)$$

Eq. (15) can be re-written as follows:

$$\{\gamma_{k+1}\} = [A]\{\gamma_k\} + [B]\{\psi_k\},$$

$$\{r_k\} = [C]\{\gamma_k\} + [D]\{\psi_k\},$$

$$[A] = e^{[A_c]\Delta t},\quad [B] = [A - I][A_c]^{-1}[B_c]. \qquad (16)$$

3. The Stability Lobe Diagram and Time Domain Analysis

In general, the chatter mechanism consists of three types of self-excited vibrations: regenerative chatter, mode coupling, and falling characteristics of cutting force. Among these types, the regenerative chatter is most often treated in the literature. A theoretical analysis is provided which is analogous to the other cutting process explained elsewhere. The analysis takes into account some features specially for grinding. Several assumptions and simplifications are made in this study, mainly:

a) The structural weakest parts of a grinding machine are usually the grinding wheel and worktable. They are the source of vibration as well as the focal points of the analysis for the dynamics characteristics in which the grinding machine is treated as a vibratory system (Fig. 1).
b) As the basic principle regenerative chatter is assumed acting in the closed-loop between the grinding process and the vibratory system of the machine (similar to the turning process model used in Fig. 3 of Ref. [4]).
c) The grinding process takes place in one plane.
d) The variable component of the grinding force depends only on vibration in the direction normal to the cutting surface. The grinding force varies proportionally and instantaneously with the variation of chip thickness.
e) A linear vibration system is assumed. The flexibility of the grinding wheel is taken into account by assuming that the grinding force is acting at the both ends of a linear spring between the grinding wheel and the workpiece. The variation of the depth of cut and the grinding force are assumed to be linear.
f) The frequency of the vibration and the mutual phase shift of undulations in subsequent overlapping cuts are not influenced by the relationship of wavelength to the length of cut
g) It is also assumed that the grinding wheel is in contact with the workpiece all the time during machining. This assumption is valid for at least the greatest part of rough grinding. With this assumption the linearity of the vibration to grinding force relation is preserved.

Suppose that a workpiece is an elastic component which is in the traverse direction and the cutting force $f(t)$ in the feed direction induces the workpiece to vibrate, the so-called chatter. Also, the surface of the workpiece is assumed smooth before machining. Due to the elastic vibration effect, the surface of the workpiece may exhibit waviness after being machined. In the next turn or cut, both the inner and outer surface of the workpiece will generate waviness, where the inner waviness is caused by tool's cutting, which is called the inner modulation $r(t)$, while the outer waviness is due to the vibration caused by previous turn cut, which is called the outer modulation $r(t - \tau)$. Therefore, the resulting chip thickness is not a constant; instead, it is a function of vibration frequency and workpiece speed. Tobias introduced the concept of the stability lobe diagram in 1965 [17].

The stability lobe diagram has been widely used to describe the dynamic characteristics of cutting process for machine tools as well as a useful tool to predict the cutting stability during planning stage of machining. One of the important properties of the stability lobe diagram is that the stability lobe represents a "convex" relationship between the cutting speed (the rotational velocity of the workpiece or the spindle) and the width of cut with maximum stability b_{lim}. When the machining occurs in the zone under the convex envelope in the stability lobe diagram the machining process is stable. The position of the envelope is relevant to the tool's material, geometry and material of workpiece. The convex shape indicates a higher stability (i.e., larger b_{lim}) under some spindle speeds, and it can be obtained by using the equation [1, 14, 15] as follows:

$$b_{lim} = \frac{-1}{2K_f \cos(\beta)\,\mathrm{Re}[G(\omega)]},$$

$$\frac{f_c}{\Omega} = N + \frac{\varepsilon}{2\pi},\quad \varepsilon = 2\pi - 2\tan^{-1}\left(\frac{\mathrm{Re}[G(\omega)]}{\mathrm{Im}[G(\omega)]}\right). \qquad (17)$$

where K_f is the specific force (N/mm^2), β is the angle between the cutting force and the normal force generating from the surface of workpiece (in this study, the worktable is assumed infinitely stiff in tangential direction, i.e. $\beta = 0$); $G(\omega)$ is the system frequency response function; N is the integer number of waves of vibration imprinted on the workpiece surface in one revolution, and $\varepsilon/2\pi$ is any additional fraction of a wave, where ε is the phase (rad) between current and previous tool vibrations; f_c is the chatter frequency; Ω is the spindle velocity (cps, rev/s).

In a regenerative chatter model, the dynamic chip thickness can be expressed as follows:

$$h(t) = h_o - \left[r(t) - r(t-\tau) \right]. \quad (18)$$

In Eq. (18), h_0 is the theoretical chip thickness, which is the same as the feed rate in the machine tool. $[r(t) - r(t - \tau)]$ is a dynamic chip thickness produced due to vibrations at the present time t and one spindle revolution period (τ) before. The dynamic cutting force can be expressed as follows:

$$f(t) = K_f b_w \left[h_o + r(t-\tau) - r(t) \right]. \quad (19)$$

Where b_w is the width of cut. Suppose that the system is a system with multiple degrees of freedom as shown in Eq. (7). With the excitation force in Eq. (19), a time domain based analysis and simulation can be performed by using Eq. (16), which is discretized from its continuous time system counterpart.

A numerical integration procedure for the time delay differential equations is based on the PIM (precise integration method) approach [23].

III. NUMERICAL ANALYSIS AND DISCUSSION

The coefficient of merit (CoM) is one of the important indicators to measure the structural stability of machine tools. There exists a close relationship between the CoM and the MNRPODC. This study utilizes MNRPODC to evaluate the cutting stability of the dynamically loaded worktable on elastic supports.

1. Parameters Setting of Dynamically Loaded Worktable

The related data used in Fig. 1 is described as follows. The span *sp* between these two supports is 0.7 m. The left and right springs k_L, k_R are the same, which is 7.5E7 N/m, and the damping coefficients, c_L, c_R are the same, which is 750 Ns/m. The mass of grinding wheel m_1 is 2.5 kg. The interface parameters are as follows: the bearing supported stiffness k_1 of the spindle is 6.9E7 N/m, and the damping c_1 is 690 Ns/m, The contact stiffness k_g between the grinding wheel and the elastic beam is 6E6 N/m and the contact damping c_g is 60 Ns/m, the length of the worktable: L = 1.4 m, the material Young's modulus: E = 2.07E11 Pa, the density: ρ = 7.8E3 kg/m^3, the cross section area of the free-free beam: A = 0.01374 m^2 (0.07 m × 0.196 m), the cross section area moment of inertia: I = 5.61E-6 m^4, the beam damping: c_B = 1750 Ns/m^2, the mass of the worktable is approximately 150 kg. The analysis is mainly based on the parameters associated with this prototype model; additionally, assume that there are 10 elastic modes of the beam, then there are 13 generalized coordinates in the system, which are denoted by $\{\gamma_1\}^T$ = $\{y_1, q_1, \ldots, q_{10}, q_H, q_S\}$, respectively. The analysis and discussion are described as follows.

2. Theory Verification

The concept is based on the following scenario. When the cutting point is at the initial position ($\xi = L/2$), and as the worktable moves toward one direction for a certain distance, the tool maintains contact with the workpiece and there exists a pair of unit force (F = 1) with same magnitude but opposite directions between the tool and the workpiece (as shown in Fig. 1). The evaluation of the response and the dynamic characteristics associated with the relative displacement generated between the tool and the workpiece is similar to the analysis of the dynamic model of changing position after the grinding wheel module and the support spring of worktable module move toward the other direction for the same distance. This analysis is, however, only applicable when the worktable is moving within the range $sp/2 \le \xi \le (L - sp/2)$; otherwise, the structure will become unstable (i.e., the worktable moves out of the left or right support spring).

The model of a prototype with rigid-worktable, also developed by the author, was used to verify the proposed theory through numerical analysis. As described in the literature [4], this model is a set of system equations with three degrees of freedom and the setting of the system parameters are as follows: as Fig. 2 in the literature [4], the mass of worktable: m_2 = 150 kg; the rotational inertia of worktable: J_1 = 24.56 kg.m^2; the damping of worktable: c_B = 0 Ns/m^2; the stiffness of bearing support: k_3 = 6.9E7 N/m; the damping of bearing support: c_3 = 690 Ns/m; a_0 = -0.35 m; b_0 = 0.35 m. Three cases are considered, they are: (a) when the worktable is at the center position (L_x = 0.0 m); (b) when the worktable moves toward the left (L_x = 0.1 m); (c) when the worktable moves toward the right (L_x = -0.1 m), and the parameters of the left and right support springs are different (where k_1 = 12.5E7 N/m, c_1 = 1250 N/m, k_2 = 7.5E7 N/m, and c_2 = 750 Ns/m). The analysis results in Fig. 2 and Fig. 3 show that the first three natural frequencies and their MNRPODC in the rigid beam model are nearly identical to that in the elastic beam model. This indicates that the concept used in this study is valid.

3. Static Stiffness Analysis

Once the worktable moves to a position ξ, a pair of loads having the same magnitude but in opposite direction is introduced between the grinding wheel and the workpiece. The system static stiffness k_s which is defined as the reciprocal of the relative displacement generated between the grinding wheel and the workpiece can be obtained by the analysis shown below.

When ω = 0, and there is no inertia force and damping force, the system of equations of motion (Eq. (7)) can be simplified as:

$$[K]\{\gamma_1\} = \{f\} = \{\psi\}. \quad (20)$$

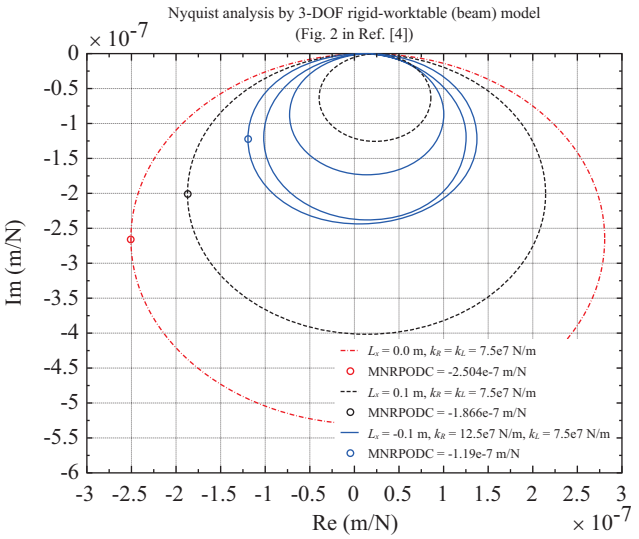

Fig. 2. The Nyquist plots by 3-DOF rigid beam [4] for the specific cases.

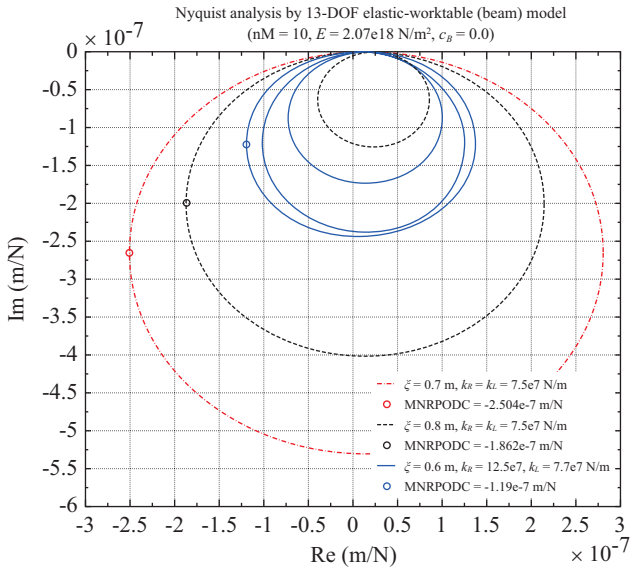

Fig. 3. The Nyquist plots by 13-DOF elastic beam model for the same conditions as Fig. 2 cases.

And the response of the system in the machining is:

$$1/k_s = r(\xi,t) = \{\psi(\xi)\}^T \{\gamma_1\}$$

$$= \phi_S(\xi) q_S(t) + \phi_H(\xi) q_H(t) - y_1(t) + \sum_{i=1}^{n} \phi_i(\xi) q_i(t). \qquad (21)$$

The result of the above equation shows that the static stiffness and the parameter k_g are related to the worktable position ξ. As shown in Fig. 4, the curves are symmetric to the center of the worktable (ξ = 0.7 m) and is slightly rippled with nearly fixed value. The values of static stiffness are maximum at both ends (ξ = 0.35 m and ξ = 1.05 m). All the

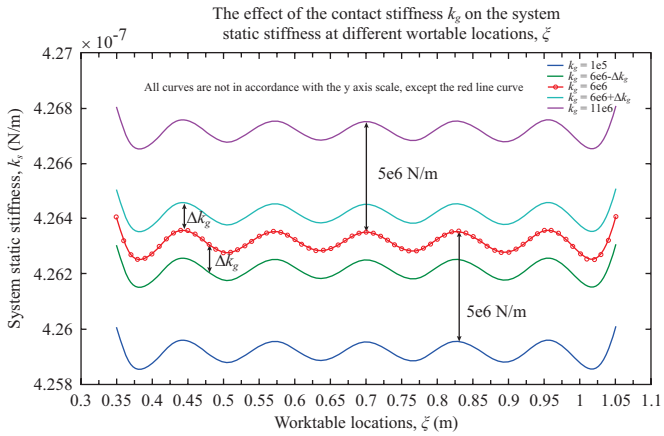

Fig. 4. The correlation between the k_s and ξ for various k_g.

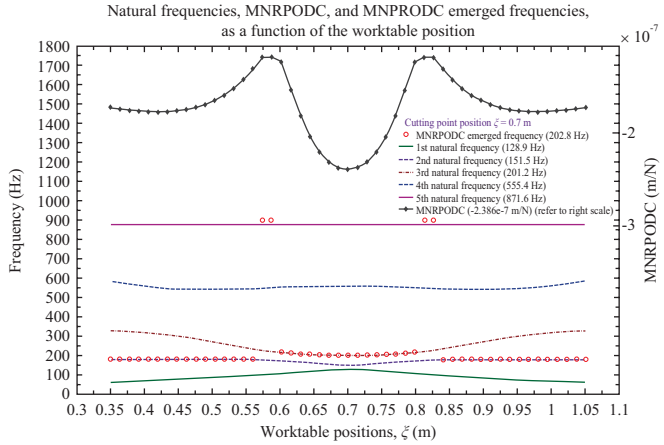

Fig. 5. MNRPODC, natural frequencies and MNRPODC emerged frequency, as a function of ξ.

curves except the one in red color are not shown in accordance with the true scale in this figure, but they are all equally spaced with Δk_g.

4. Dynamic Performance Analysis

With *sp* = 0.7 m (i.e. the feasible range: 1.05 m ≥ ξ ≥ 0.35 m), as the worktable moves along different positions, based on the parameters for the prototype model, the first five natural frequencies of the system, the MNRPODC performance curve, and the MNRPODC emerged frequency are computed, The results are shown in Fig. 5 and a detailed discussion of the results is noted below.

a) The trend of the MNRPODC performance curve is closely related to the natural frequency and the MNRPODC emerged frequency. As shown in Fig. 5, all curves are symmetric to the center of the worktable (i.e., ξ = 0.7 m), and all natural frequencies, except for the fifth frequency that only has a minimal change, change as the worktable moves to a different location. The change in the MNRPODC emerged frequency, as the frequency

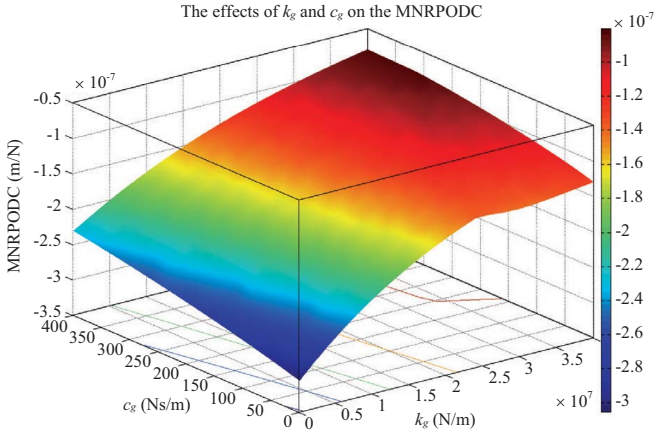

Fig. 6. Correlation of the system dynamic compliance, contact stiffness, and contact damping.

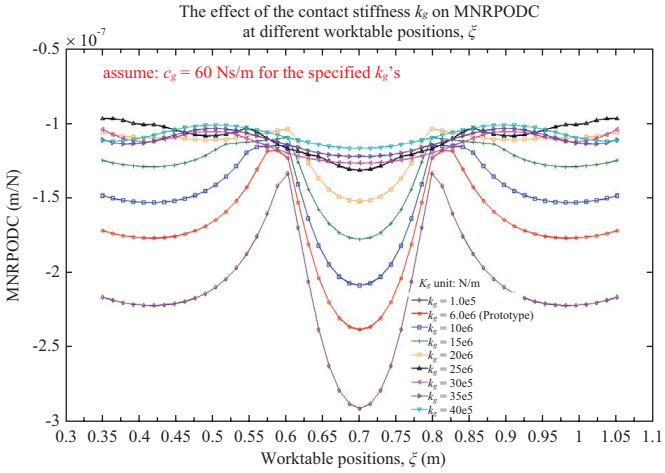

Fig. 7. The effect of the k_g on MNPRODC at different worktable positions ξ.

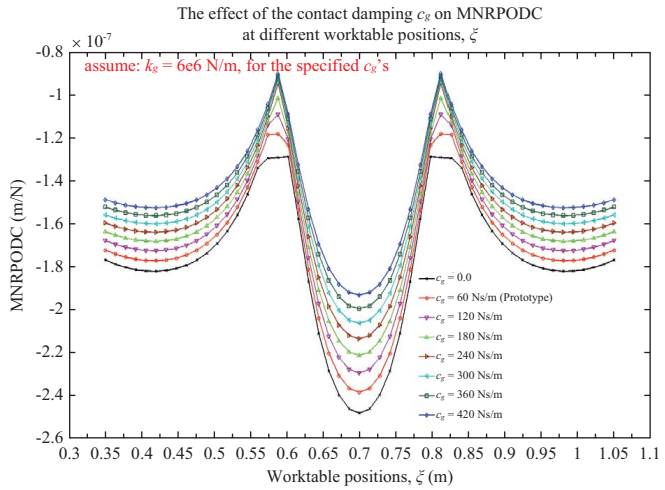

Fig. 8. The effect of the c_g on MNPRODC at different worktable positions ξ.

hops from one to another, is the key reason that causes the MNRPODC curve to change significantly. All the MNRPODC emerged frequencies are slightly higher than any natural frequencies in the system.

b) The center part of the MNRPODC performance curve (0.798 m ≥ ξ ≥ 0.602 m) is concave, and the MNRPODC emerged frequency on this part is slightly higher than the third natural frequency. The center of the MNRPODC curve usually has the lowest value. At this center, the first frequency (128.9 Hz) and the second frequency (151.5 Hz) are the closest with only 22.6 Hz apart, and the structure is the least stable (prone to chatter). This result is different from the frequency difference obtained in a similar but rigid model analysis [4], which is nearly 0 Hz.

c) In addition to the concave at the center part, at the left and right part of the MNRPODC curve, there exists a respective peak connecting smoothly toward two sides. The main reason is as follows. The MNRPODC emerged frequency, starting from the two sides (0.56 m ≥ ξ ≥ 0.35 m and 1.05 m ≥ ξ ≥ 0.84 m), hops from the frequency slightly higher than the second frequency up to the frequency slightly higher than the fifth frequency at two parts (0.588 m ≥ ξ ≥ 0.574 m and 0.826 m ≥ ξ ≥ 0.812 m), followed by hopping down to the frequency slightly higher than the third frequency at the center part (0.798 m ≥ ξ ≥ 0.602 m).

5. The Effects of k_g and c_g on the System Performance MNRPODC

When the cutting point is at the initial position (ξ = L/2), Fig. 6 shows the 3D diagram of the correlation of k_g – c_g – MNRPODC where the contact stiffness k_g increases from 1E5 N/m to 4E7 N/m, and the contact damping c_g increases from 0 Ns/m to 400 Ns/m. The result shows that if k_g and become larger, the |MNRPODC| becomes smaller, which indicates that the structure is more stable with better cutting performance. The description is as follows.

a) When c_g is 60 Ns/m, Fig. 7 shows the effect of the contact stiffness k_g on the system performance, at different worktable positions. As shown in the figure, the MNRPODC curve increases as the contact stiffness increases. Specifically, when k_g = 6E6 N/m, the correlation of the system dynamic performance, the natural frequency, and the MNRPODC emerged frequency is the same as in Fig. 5, and the behavior of other curves with different k_g is similar.

b) When k_g = 6E6 N/m, Fig. 8 shows the effect of the contact damping c_g on the system performance, at different worktable positions. As shown, the system performance MNRPODC curve increases as the contact damping increases; that is, the performance of the MNRPODC curve improves as the contact damping increases.

6. Chatter Stability Lobes [1, 2, 15]

Fig. 9 shows the 3D stability lobe diagram of the correlation

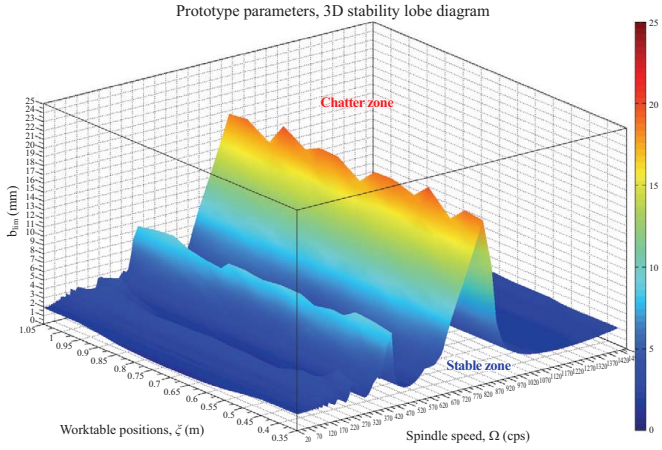

Fig. 9. Three-dimensional stability lobe diagram for Ω – b_{lim} – ξ.

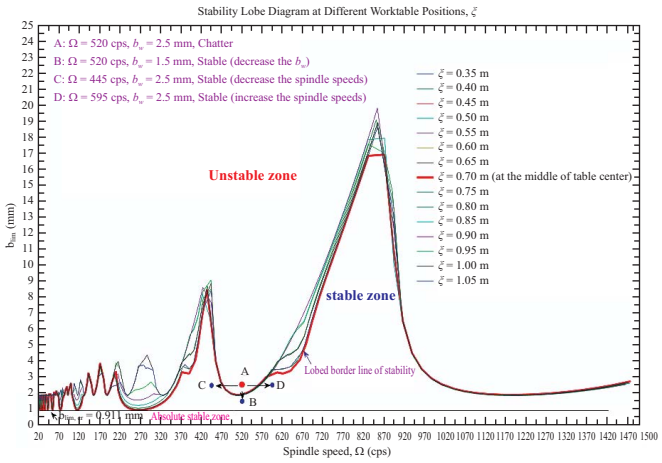

Fig. 10. Stability lobe diagrams for various ξ.

of Ω – b_{lim} – ξ, where the hard spots on the workpiece are assumed to generate regenerative chatter effect, as described in the above theory, and the computation is based on the prototype parameters with the cutting force coefficient K_f = 2.3 E9 N/mm^2 (1035 carbon steel) [14, 15]. In this figure, the chatter zone is above the outer curve surface and the stable zone under the inner curve surface. The description is as follows.

a) The view along the ξ axis from Fig. 9 and Fig. 10, comprising the stability lobe diagram with various ξ, shows that when the worktable is within the range 1.05 m ≥ ξ ≥ 0.35 m, the area above all lobe curves is the chatter zone, and the area below all lobe curves is the stable zone. The area below b_{lim} = 0.911 mm is the absolute stable zone because no chatter is generated for any spindle speed. When worktable position is at ξ = 0.7 m, the MNPRODC is the minimum (-2.386E-7 m/N), and the MNPRODC emerged frequency is 202.8 Hz, which is slightly higher than the third natural frequency, which is 201.2 Hz. As shown in Fig. 5, the first frequency and the second frequency are the closest, and The limiting critical width $b_{lim,cr}$ for any spindle speed can be directly obtained with $b_{lim,cr} = 1/(2 \times K_f \times |\text{MNPRODC}|_{max})$.

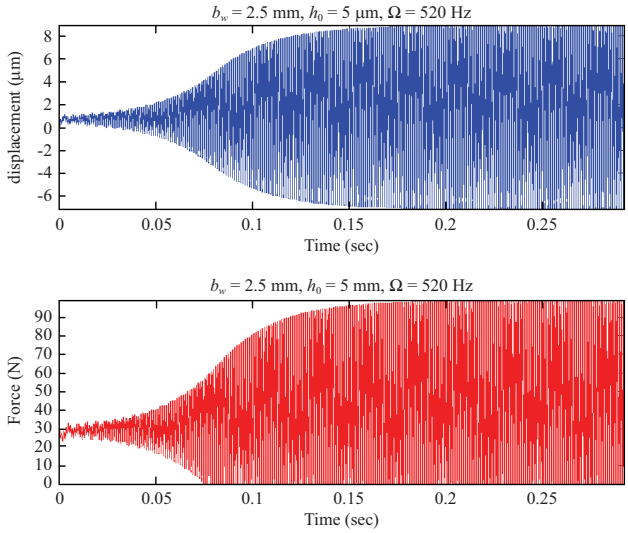

Fig. 11. Time domain displacement and force for b_w = 2.5 mm, h_0 = 5 μm, Ω = 520 cps. (unstable point A in Fig. 10)

b) As shown in Fig. 10, point A is located in the chatter zone. Moving point from A to point B, C, or D, which holds stable cutting conditions, can suppress chatter and thus improve machining efficiency. This observation is verified by the time-domain analysis as follows.

7. Time Domain Simulation [14]

If the cutting force is based on the above-mentioned regenerative chatter effect, then its solution is determined by the present and previous vibration, i.e., $r(t)$ and $r(t - \tau)$ in the dynamic equations. Therefore, the chatter representation equation is a time delay differential equation. However, if the vibration is too large, that is $[r(t) - r(t - \tau)] > h_0$, then the tool may jump out resulting in zero cutting thickness and zero cutting force. Additionally, due to the tool jumping out, the effect of vibration waviness on the workpiece, caused by the last turn, on the computation of present cutting thickness becomes more complex (i.e., multiple regenerative effect) Fig. 10 shows all the lobes generated within worktable position range 1.05 m ≥ ξ ≥ 0.35 m, based on the prototype parameters, where point A is located in the chatter zone, and point B, C, and D are in the stable zone, respectively. Fig. 11 shows the time-domain analysis of the waviness on the workpiece surface and the cutting force at point A with operating condition b_w = 2.5 mm, h_0 = 5 μm, Ω = 520 cps, and as shown in the figure, the results are divergent.

In Fig. 12, the results of the time-domain analysis of the waviness on the workpiece surface and the cutting force at point B with operating condition b_w = 1.5 mm, h_0 = 5 μm, Ω = 520 cps are stable and convergent. Fig. 13 shows that the results are stable and convergent regarding the time-domain

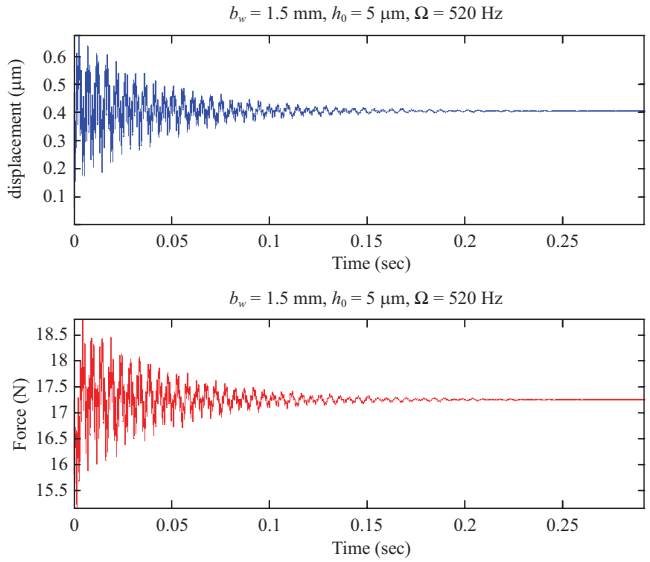

Fig. 12. Time domain displacement and force for b_w = 1.5 mm, h_0 = 5 μm, Ω = 520 cps. (stable point B in Fig. 10)

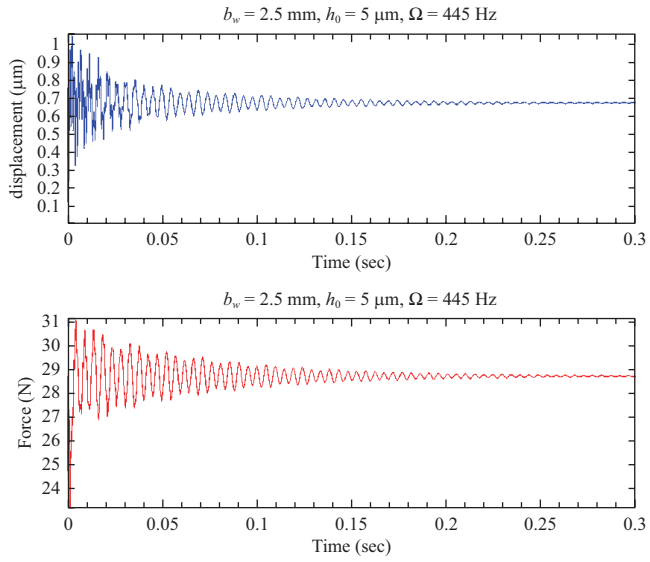

Fig. 13. Time domain displacement and force for b_w = 2.5 mm, h_0 = 5 μm, Ω = 445 cps. (stable point C in Fig. 10)

analysis of the waviness on the workpiece surface and the cutting force at point C, under operating condition b_w = 2.5 mm, h_0 = 5 μm, Ω = 445 cps. Fig. 14 shows that the results of the time domain analysis of the waviness on the workpiece surface and the cutting force at point D are stable and convergent, under operating condition b_w = 2.5 mm, h_0 = 5 μm, Ω = 595 cps. These simulation results verify the cutting stability and suggested some measures to work around chatter during the cutting process: by reducing the width of cut (point B), by reducing speed (point C), and by increasing speed (point D). Additionally, these measures can be used to prevent chatter.

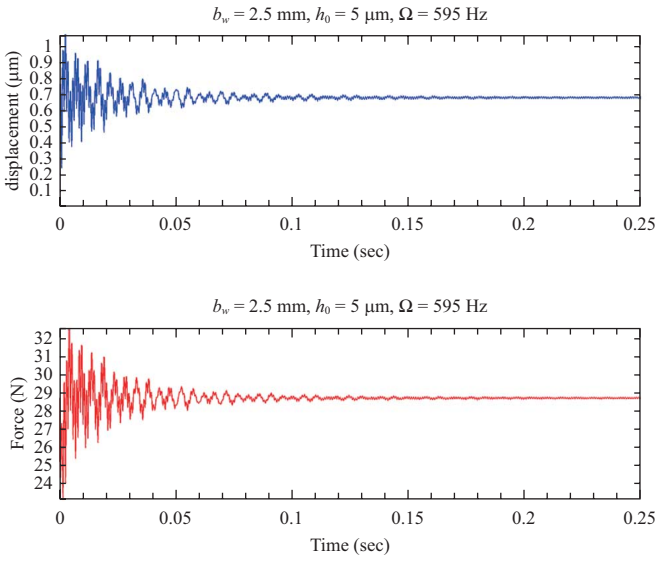

Fig. 14. Time domain displacement and force for b_w = 2.5 mm, h_0 = 5 μm, and Ω = 595 Hz (Stable point D in Fig. 10).

IV. CONCLUSION

This study propose a procedure to evaluate the dynamic performance and the cutting stability of a dynamically loaded worktable on elastic supports in a surface grinder. By combining the Lagrange energy method with the technique of assumed mode expansion that superposing the elastic and rigid body modes of a free-free beam, the system dynamic equations in a symbolic form are derived. The |MNRPODC| and the b_{lim} are used as the performance indicators to evaluate the effect of the parameters, such as the contact stiffness and the contact damping between the tool and the workpiece, on system performance. The structural static and dynamic characteristics of the dynamically loaded worktable under various positions and the stability are also analyzed. Major results are summarized as follows:

a) Although the equations of motion for the models of the elastic-worktable and rigid-worktable are not the same, their numerical simulation results, under some conditions, are very similar. This validates the system of equations derived in this study. However, the analysis is only applicable when the worktable is moving within the range $sp/2 \le \xi \le (L - sp/2)$; otherwise, (i.e., the worktable moves out of the left or right support spring), the structure becomes unstable.
b) The contact stiffness k_g increases or reduces Δk_g, the static stiffness at any position increases or reduces Δk_g at the same time. The behavior is the same as the fixed value in the analysis of the rigid model [4] except having slightly rippled with nearly fixed value.
c) In general, if the contact stiffness k_g increases, the static stiffness of the worktable increases and the performance of the MNRPODC curve within the moving range of the

worktable increases; additionally, if the contact damping c_g increases, the performance of the MNRPODC curve within the moving range of the worktable increases accordingly. Both k_g and c_g have significant impact on the improvement of system stability.

d) The trend of the MNRPODC performance is closely related to the system natural frequency and the MNRPODC emerged frequency. The MNPRODC performance curve in the prototype model changes depending on the location of the worktable. The center part of the curve is concave and the curve is symmetric to the center. The limiting critical width $b_{lim,cr}$ for any spindle speed in the absolutely stable zone of the Lobe diagram can be obtained with $b_{lim,cr} = 1/(2 \times K_f \times |\text{MNPRODC}|_{max})$.

e) Stability lobe diagram may clear up the complex overlapping in the curves between the chatter zone and stable zone. The cutting stability was verified by time domain analysis. Additionally, from the lobe diagram, the proper operating range can be determined, for example, increase of width of cut or speed with avoidance of chatter zone, shall improve machining efficiency effectively.

NOTATION

A	cross-sectional area of beam (m^2)
$[A_c]$	the continuous time system matrix
a_0	parameter between k_1 and the mass centre of the worktable at location $L_x = 0$ (m) as Fig. 2 in Ref. [4]
b_0	parameter between k_2 and the mass centre of the worktable at location $L_x = 0$ (m) as Fig. 2 in Ref. [4]
b_{lim}	the limiting chip width (m)
$b_{lim,cr}$	the limiting critical chip width for any spindle speed (m)
b_w	the chip width (m)
$[B_c]$	the continuous time input matrix
$[C]$	damping matrix (Ns/m)
$[C_c]$	the output matrix
c_1	the equivalent bearing damping (Ns/m)
c_B	the beam damping (Ns/m^2)
c_g	the contact damping between the grinding wheel and the workpiece (Ns/m)
c_L, c_R	the damping of the left and right supports (Ns/m)
$[D_c]$	the direct transmission matrix
E	the Young's modulus (N/m^2)
$\{f\}$	force vector
f_c	the chatter frequency (Hz)
$G(\omega)$	the oriented transfer function between the tool and workpiece
h_0	the mean chip thickness, or commanded feed per revolution for the grinding (μm)
I	moment of inertia of beam cross-section about bending axis (m^4)
Im(G)	the imaginary of the oriented transfer function between the tool and workpiece
L_x	movement location of the mass centre of the worktable to the origin (m) as Fig. 2 in Ref. [4]
$[K]$	stiffness matrix (N/m)
K_f	the specific force or cutting force coefficient (N/mm^2)
k_1	the equivalent bearing stiffness (N/m)
k_g	the contact stiffness between the grinding wheel and the workpiece (N/m)
k_L, k_R	the spring constants of the left and right supports (N/m)
k_s	the static stiffness between the tool and workpiece (N/m)
L	length of beam (m)
MNRPODC	the maximum negative real part of the overall dynamic compliance
m_1	mass of the grinding wheel (kg)
$[M]$	mass matrix (kg)
N	the largest possible integer such that $\varepsilon/2\pi < 1$
R	the damping dissipated energy of the system (Nm)
Re(G)	the real part of the oriented transfer function between the tool and workpiece
$\{r\}$	output vector
sp	span between supports (m)
T	the kinetic energy of the system (Nm)
t	time (sec)
U	the potential energy of the system (Nm)
y_1	displacement of mass center of the grinding wheel (m)
$y(\xi, t)$	transverse displacement (m)
Ω	the spindle speed (cps)
ε	the phase (rad) between current and previous tool vibrations
τ	period between two cuts (s)
ω	angular velocity (rad/s)
ξ	a coordinate along the neutral axis of the beam (m)
ρ	mass density of beam (kg/m^3)
$\phi(\xi)$	normalized eigenfunction ($m^{-1/2}$)
$\phi_H(\xi)$, $\phi_S(\xi)$	normalized translation and rotation eigenfunction of rigid beam
$\{\psi(\xi)\}$	tie vector
$\{\kappa(\xi)\}$	support vector
$\{\gamma\}$	the state vector
$\{\gamma_1\}$	generalized coordinate vector ($m^{3/2}$)
$\delta_{j,k}$	Kronecker delta
λ_i	roots of frequency equation for free-free beam

ACKNOWLEDGMENTS

This work was supported by the National Science Council of, the Republic of China, under the contract number: NSC 100-2221-E-182-045.

REFERENCES

1. Altintas, Y., *Manufacturing Automation: Metal Cutting Mechanics, Machine Tool Vibrations, and CNC Design*, Cambridge University Press, pp. 65-116 (2000).
2. Altintas, Y., "Analytical prediction of three dimensional chatter stability in milling," *JSME International Journal*, Vol. 44, No. 3, pp. 717-723 (2001).
3. Argento, A. and Scott, R. A., "Dynamic response of a rotating beam subjected to an accelerating distributed surface force," *Journal of Sound and Vibration*, Vol. 157, No. 2, pp. 221-231 (1992).
4. Cha, K. C., Wang, N. Z., and Liao, J. Y., "Dynamics and stability analysis of the simplified model for the surface grinder in various worktable positions," *Proceedings of the Institution of Mechanical Engineers, Part K: Journal of Multi-body Dynamics*, Vol. 225, No. 3, pp. 220-234 (2011).
5. Esmailzadeh, E. and Jalilib, N., "Vehicle-passenger-structure interaction of uniform bridges traversed by moving vehicles," *Journal of Sound and Vibration*, Vol. 260, pp. 611-635 (2003).
6. Fryba, L., *Vibration of Solids and Structures under Moving Loads*, Thomas Telford, pp. 103-128 (1999).
7. Gu, U. C. and Cheng, C. C., "Vibration analysis of a high-speed spindle under the action of a moving mass," *Journal of Sound and Vibration*, Vol. 278, pp. 1131-1146 (2004).
8. Hwang, R. M. and Cha, K. C., "Construction of a prediction model for the structural stability of a surface grinder using backpropagation neural network," *The International Journal of Advanced Manufacturing Technology*, Vol. 37, No. 11-12, pp. 1093-1104 (2008).
9. Ju, S. H., Lin, H. D., Hsueh, C. C., and Wang, S. L., "A simple finite element model for vibration analyses induced by moving vehicles," *International Journal for Numerical Methods in Engineering*, Vol. 68, No. 12, pp. 1232-1256 (2006).
10. Katz, R., Lee, C. W., Ulsoy, A. G., and Scott, R. A., "The dynamic response of a rotating shaft subject to a moving load," *Journal of Sound and Vibration*, Vol. 122, No. 1, pp. 131-148 (1988).
11. Kelly, S. G., *Fundamentals of Mechanical Vibrations*, McGraw-Hill, pp. 455-506 (2000).
12. Lee, H. P., "Dynamic response of a Timoshenko beam on a Winkler foundation subjected to a moving mass," *Applied Acoustics*., Vol. 55, No. 3, pp. 203-215 (1998).
13. Mackertich, S., "The response of an elastically supported infinite Timoshenko beam to a moving vibrating mass," *Journal of the Acoustical Society of America*, Vol. 101, No. 1, pp. 337-340 (1996).
14. Schmitz, T. L. and Smith, K. S., *Machining Dynamics: Frequency Response to Improved Productivity, Springer*, pp. 66-67, 85-94 (2009).
15. Tlusty, J., *Manufacturing Processes and Equipment*, Prentice Hall, pp. 560-594 (2000).
16. Tlusty, J. and Moriwaki, T., "Experimental and computational identification of dynamic structural models," *Annals of the CIRP*, Vol. 25, pp. 497-503 (1976).
17. Tobias, S. A., *Machine Tool Vibration*, Blackie & Son, pp. 143-332 (1965).
18. Wang, F. Y., *Physics with MAPLE: The Computer Algebra Resource for Mathematical Methods in Physics*, John Wiley & Sons, pp. 71-100 (2008).
19. Weck, M., *Handbook of Machine Tools - Metrological Analysis and Performance Tests*, Vol. 4, John Wiley & Sons, pp. 46-61 (1984).
20. Yoshimura, M. "Study on optimum design of machine structures with respect to dynamic characteristics," *Bulletin of the Japan Society of Mechanical Engineer*, Vol. 145, No. 20, pp. 811-818 (1977).
21. Yoshimura, M., "Design sensitivity analysis of frequency response in machine structures," *Journal of Mechanisms, Transmissions, and Automation in Design*, Vol. 106, No. 1, pp. 119-125 (1984).
22. Zhang, G., Huang, Y., Shi, W., and Fu, W., "Predicting dynamic behaviors of a whole machine tool structure based on computer-aided engineering," *International Journal of Machine Tools and Manufacture*, Vol. 43, No. 7, pp. 699-706 (2003).
23. Zhong, W. X., *Duality System in Applied Mechanics and Optimal Control*, Kluwer Academic Publishers, pp. 4-10 (2004).